Physics and Imaging in Radiation Oncology 27 (2023) 100463

Contents lists available at ScienceDirect

Physics and Imaging in Radiation Oncology

journal homepage: www.sciencedirect.com/journal/physics-and-imaging-in-radiation-oncology

Original Research Article

Using density computed tomography images for photon dose calculations in radiation oncology: A patient study

Camille Decoene *, Frederik Crop

Medical Physics, Centre Oscar Lambret, Lille, France

ARTICLE INFO

Keywords:
HU conversion
Mass density
Dose calculation

ABSTRACT

Background and purpose: Conventional workflows for dose calculations require conversions between Hounsfield Units (HU) and the mass or electron density for Computed Tomography (CT) images in the Treatment Planning System (TPS). These conversions are scanner– and mostly kVp–dependent. A density representation or reconstruction at the CT level can potentially simplify the workflow. This study aimed to investigate the agreement between these two methods for patients and different calculation algorithms.

Materials and methods: Density conversions for conventional HU–density conversions were first established using two phantoms with appropriate inserts. Next, the differences in density and dose calculations between both methods were assessed using 95% Limits of Agreement (LOA) Bland–Altman analysis for 44 consecutive clinical patient cases. These cases represented a mix of indications, algorithms (collapsed cone, convolution superposition, ray tracing, finite–size pencil beam, and Monte Carlo), and scan kVp (80 to 140) in two different commercial TPS.

Results: No statistically significant bias in density or dose calculations was found between the two methods. Furthermore, 95% LOAs between both methods were ± 0.05 g/cm^3 and ± 0.1 Gy for density and dose, respectively. Small but clinically irrelevant dose differences were found in high–density gradient regions for convolution superposition calculations or CT scans with non-delayed contrast agent injections with targets nearby vessels.

Conclusions: The in vivo density–reconstructed images at the CT level were assessed to be equivalent. Therefore, they can simplify and improve clinical workflows, allowing patient–specific acquisitions for contouring and density–reconstructed images for dose calculations.

1. Introduction

A frequently used workflow for dose calculations (Fig. 1, upper line) requires a calibration curve based on a Computed Tomography (CT) image with calibrated inserts. This establishes the CT numbers corresponding to the relative electron density (RED) or mass density (MD) curves. These curves are subsequently used to convert CT numbers to electron or mass densities for patients [1,2]. In clinical practice, specific acquisition kVp, such as 80 kVp for pediatrics, 140 kVp for large patients, or a combination for dual–energy CT can be useful for better image quality [3]. Therefore, two solutions are often applied: a) always acquire an additional 120 kVp CT with a specific filter for dose calculations and/or b) establish CT numbers corresponding to MD curves for all energies and filters available to use any energy (Fig. 1, upper line). The former solution (a) can result in registration issues due to patient movement, respiration or peristaltic movements between the two CTs. The latter solution (b) requires an extensive range of measurments and possibly misattribution of curves when manually attributed in the TPS. The former solution also allows acquisition without contrast agent. However, the presence of contrast agent generally leads to very low dose differences [4,5].

Another, less frequently, applied method (c) is binning into the chemical composition of human tissue [6–8], thus removing the need for extensive CT characterization. This method uses detailed material composition for attenuation and stopping powers and allows dose to medium or water in medium calculations [9]. However, this binning has the downside of not characterizing the scanner and possibly introducing issues with phantom representations and dose calculations, especially acrylic phantoms. This combination results in almost the same uncertainty level in human tissues [6].

* Corresponding author at: Service of Medical physics, Centre Oscar Lambret, 3, Rue Frédéric Combemale, Lille 59000.
E-mail address: C-Decoene@o-lambret.fr (C. Decoene).

https://doi.org/10.1016/j.phro.2023.100463
Received 21 March 2023; Received in revised form 20 June 2023; Accepted 20 June 2023
Available online 24 June 2023

In this study, a fourth method (d) was investigated [10–13] for patients. Instead of conversion at the Treatment Planning System (TPS) level, it can already be performed directly on the acquired CT by generating a density image through a specific imaging filter or kernel (Fig. 1, lower line). Based on Flatten et al.'s investigation on phantoms [10], this method can lead to uncertainties comparable to those of other methods. It can potentially solve the practical and safety issues associated with the most frequently applied method (the first method). However, it must be cautiously performed when combined with dual–energy CT [11]. It may also offer more robust results for proton dose calculations [12]. Finally, it simplifies using small field–of–view (FOV), kV–optimized images for contouring and large FOV MD images for dose calculations. This study aimed to investigate the agreement between the TPS– and CT–level conversion methods for various calculation algorithms and clinical situations as the literature mainly treats phantom acquisitions, which can underestimate in vivo results.

2. Material and methods

2.1. Scanner and filters

A SOMATOM Confidence RT Pro 64 CT scanner (Siemens Healthineers, DE) was used for all image acquisitions. Five kVp were available; however, only four were clinically used: 80, 100, 120, and 140 kVp. This scanner permits using the DirectDensity® algorithm [14] to reconstruct any acquired image. DirectDensity® images were obtained by combining image–based bone detection with projection–based material decomposition. Depending on the algorithm option, CT values can also be reconstructed as RED and relative MD. For example, the Sd40 reconstruction filter provided CT values as RED, whereas Sm40 provided CT values as relative MD. Only Sm40 was considered and compared with the standard Body Regular Level 38 (Br38) reconstruction filter in this study. This Br38 filter was a standard reconstruction filter and practically considered the "kV" filter for each energy. It was recommended by Siemens and resulted in a compromise between noise, spatial resolution, and contrast for contouring.

Eq. (1) describes how CT pixel values [CT_{MD}] as relative MD are represented, equivalent to the use of the classical Hounsfield Units (HU).

$$MD = 0.001 \times CT_{MD} + 1 g/cm^3 \quad (1)$$

2.2. Treatment planning systems

Two TPSs were studied: (1) Precision/iDMS (Accuray Inc, Madison, USA), and (2) Raystation (Research Labs, Stockholm, SE). Raystation performed dose calculations using a Collapsed Cone (CC) algorithm [15], whereas Precision performed dose calculations using the Convolution Superposition (CS) algorithm for Tomotherapy®. For Cyberknife dose calculations, Ray Tracing, Finite–Size Pencil Beam (FSPB), or Monte Carlo were used. Monte Carlo calculations were performed at a 2% uncertainty level. All algorithms used MD, except Ray Tracing and FSPB required electron densities. As a conversion is performed between CT value to one of both density types, the linear relation (1) was used for MD whereas a MD-RED correction using listed MD-RED values of the Gammex inserts was introduced for the RED curve in Precision for ray tracing and FSBP.

2.3. Trueness verification on phantoms

Trueness of density conversion was first verified on two different phantoms based on the results of Flatten et al [10], but extending with a second phantom: (1) the Gammex® Tomotherapy Cheese RMI Model 467 phantom and (2) CIRSinc® Electron Density Model 062. Since the Gammex phantom was used to compute CT numbers corresponding to relative MD curves, trueness evaluation of density conversions was only performed for each insert of the CIRS phantom. These phantom results, extended to a second density phantom, were useful to assess the uncertainty due to the use of a different phantom but did not present the main subject of this study. The phantom density and dosimetric evaluation were therefore detailed in the supplementary file, S1 phantom-based trueness evaluation. More details about tissue equivalency of phantoms can be found on the work provided by Gomà et al [16].

2.4. Patients

Forty–four routine clinical cases were considered, representing various localizations, treatment techniques, and dose calculations (Table 1). Two image series were reconstructed for each patient using both the Br38 standard reconstruction and DirectDensity® Sm40 algorithms. This allowed direct pixel-to-pixel evaluation.

Three patients were scanned at 80 kVp, four at 100 kVp, 31 at 120 kVp, and six at 140 kVp. Cases 20 and 21 represented the same patient and treatment plan but were transferred between Precision and Raystation. Cases 37 and 38 represented the same patient and treatment plan but respectively calculated using planning images at 80 kVp and at 140 kVp. Informed consent was obtained from all patients for the anonymous use of data.

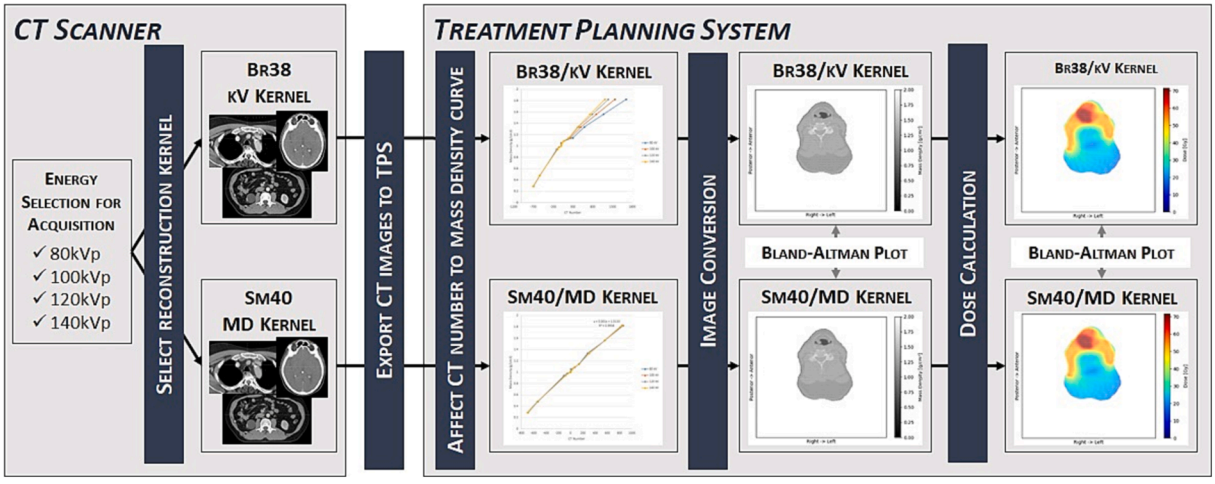

Fig. 1. Overview of the conversion methods. The upper line represents conventional workflow using multiple conversion curves for different kV applications. The lower line represents the investigated workflow with mass or electron density conversion on the CT level, resulting in a single conversion curve for all CT acquisitions.

Table 1
Summary of the fourty-four cases. RS, RayStation; Pr, Precision/iDMS; CC, Collapsed Cone; CS, Convolution Superposition; FSPB, Finite–Size Pencil Beam; RayT, Ray Tracing; MD, mass density; ED, electron density.

Localisation	Tube Voltage (kVp)	Treatment Planning System	Treatment Device	Number of Patients
Abdomen	80	RS [CC-MD]	Tomotherapy	2
	100	RS [CC-MD]	Halcyon	1
	120	PR [FSBP-ED]	Cyberknife	1
		PR [RayT-ED]	Cyberknife	2
Bone	120	PR [RayT-ED]	Cyberknife	1
		RS [CC-MD]	Halcyon	2
	140	RS [CC-MD]	Halcyon	1
		RS [CC-MD]	Tomotherapy	1
Breast	120	PR [CS-MD]	Tomotherapy	4
		RS [CC-MD]	Tomotherapy	1
		RS [CC-MD]	Halcyon	1
	140	RS [CC-MD]	Tomotherapy	1
		RS [CC-MD]	Halcyon	1
Head	80	RS [CC-MD]	Halcyon	1
	100	RS [CC-MD]	Tomotherapy	1
		RS [CC-MD]	Halcyon	1
	120	PR [FSBP-ED]	Cyberknife	1
		PR [RayT-ED]	Cyberknife	2
		RS [CC-MD]	Halcyon	1
	140	RS [CC-MD]	Halcyon	1
Head & Neck	120	PR [CS-MD]	Tomotherapy	3
		RS [CC-MD]	Halcyon	3
Lung	120	PR [CS-MD]	Tomotherapy	1
		PR [MC-ED]	Cyberknife	1
Medulloblastoma	100	RS [CC-MD]	Tomotherapy	1
	120	RS [CC-MD]	Tomotherapy	1
Oesophagus	120	PR [CS-MD]	Tomotherapy	1
	140	RS [CC-MD]	Halcyon	1
Pelvic	120	PR [CS-MD]	Tomotherapy	1
		PR [RayT-ED]	Cyberknife	1
		RS [CC-MD]	Halcyon	4

2.5. Image conversion evaluations

The image value to density conversion was implicitly performed in the TPS during the dose calculation; however, these maps were not accessible to the user. A custom Python code was created to compare density conversions for all images using the same HU–density conversions to investigate patient conversions. Therefore, density conversions for kV/Br38 images followed the measured conversion, whereas MD/Sm40 images followed the direct relation (Eq. (1)). These relative MD maps for patients were compared using pixel–to–pixel Bland–Altman plots [17–19]. In the absence of a true value, Bland–Altman plots indicate the 95% limits of agreement (LOA) between the two methods, which is explained in more detail by Giavarina [20]. In a Bland–Altman plot, the difference between methods A and B is represented as a function of the mean of methods A and B. Voxels outside the phantom or patient are highly affected by the noise; therefore, only voxels inside the phantom and patients were considered in this study. Because the number of points represented was very high, the Bland–Altman plots represented density heatmaps with hexagonal bins. These bins were shown using a log2 distribution to accentuate differences visually, even when these seldom occur. The histogram distribution for both axes was also shown in the borders to further accentuate the frequency of occurrence of differences.

2.6. Dosimetric evaluations

An evaluation was performed for dose calculations for patients. All treatments were planned based on Br38/kV images as performed in clinical practice. After plan validation by the medical physicist and the radiation oncologist, the plan was recomputed on the Sm40 Direct-Density® CT images using the CT numbers corresponding to relative MD curves. Because there was no ground truth available for dose calculations, Bland–Altman plots for the evaluation of 95% LOAs were applied for voxel–to–voxel evaluations between the two methods. Finally, the following dosimetric indices were compared for all targets and Organs at Risk (OAR): D_{2cc} for OARs, $D_{95\%}$ for Target volumes, and D_{mean} for both. For case 16, the dose grid size influence was compared by recalculating a 3 mm and 1 mm voxel size. One Precision/CS breast case (case 20) was recalculated in RayStation/CC for a direct comparison between CC and CS (case 21) by transferring the same plan from Precision/iDMS to Raystation for dose recalculation.

3. Results

3.1. Image conversion evaluations

As detailed in the supplementary files S1, the use of the CIRS or the Gammex inserts may lead to slightly different values, depending on the kV or MD reconstruction for water (1–2%) and high density inserts (4–5% density bias). This difference in trueness may lead to a small bias in dose calculations. Overall, 95% LOAs were in the order of ±0.02 g/cm^3 on phantom.

For patients, 95% LOAs between both density conversions were ±0.05 g/cm^3 without any statistically significant bias, as shown in Fig. 2. The log2 heat map shows that some differences were present, but with very low frequency. An example of a line density profile is shown in Fig. 5, where these small density differences can be found in high–density gradient regions such as interfaces/skin or lung alveoli.

3.2. Dosimetric evaluations

Fig. 3 shows in vivo dose differences with 95% LOAs of + –0.1 Gy between conventional density conversion and direct density images for all patients. Differences were visually exaggerated using a log2 scale to distinguish differences case by case. Some detailed patient evaluations are provided in the supplementary file S4.

A distinction was observed between the CC (RayStation) and CS (Precision) dose calculations, leading to slightly different 95% LOAs of [–0.08; 0.07] Gy and [–0.13; 0.16] Gy, respectively, as shown in Supplementary File S2. These differences could be thought to be attributed to the dose calculation voxel size. However, the differences between the 1 mm and 3 mm voxel sizes, as shown in Supplementary File S3, were not the origin. These differences between CC and CS were further investigated by recalculating a tomotherapy iDMS plan (CS) using RayStation (CC). This is also shown in Supplementary Fig. S4.1. For breast cases, the largest dose differences were found in high–density gradients, such as the skin, and thus buildup. Line density and dose plots are shown in Fig. 5.

The Bland Altman plots of dose indices (D_{2cc}, $D_{95\%}$ and D_{mean}) for all patients, as shown in Fig. 4, show 95% LOAs of <0.4 Gy. However, these were influenced by outliers originating from case 14, which is detailed in the discussion. As shown in the Supplementary Fig. S2, this resulted finally in a small linear bias and thus a difference in D_{mean}, D_{2cc}, and $D_{95\%}$. No significant differences were observed between 120 kV, 80 kV, 100 kV, or 140 kV results (see Supplementary Fig. S3).

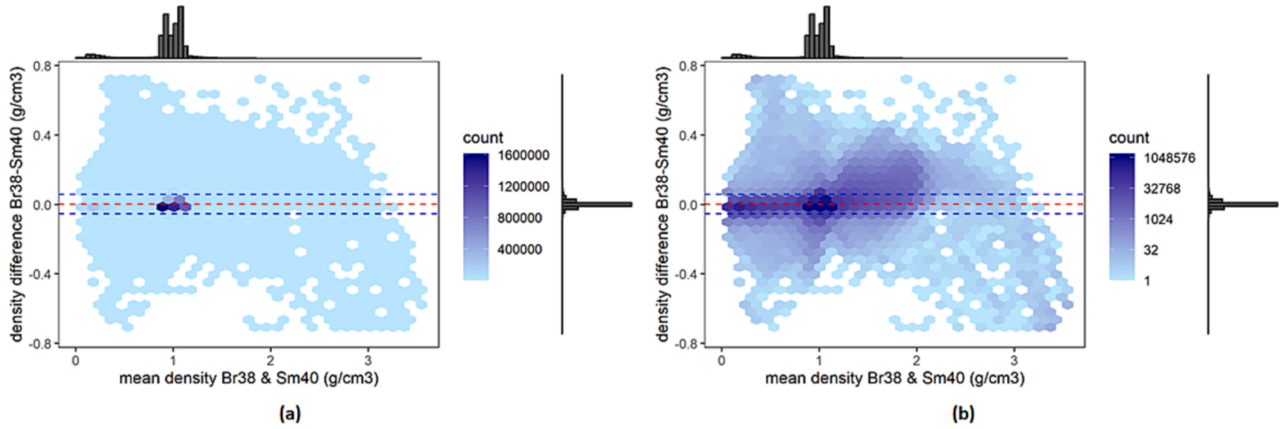

Fig. 2. Bland–Altman plots of the absolute mass density difference combined for all cases. The image (a) shows a linear scale, and the image (b) shows a log2 scale to show possible differences visually. The 95% Limits Of Agreement (+–0.05 g/cm3) between both methods are presented as blue dashed lines, whereas the absolute difference is presented as red dashed lines No statistically significant bias was found between the two investigated methods. (For interpretation of the references to colour in this figure legend, the reader is referred to the web version of this article.)

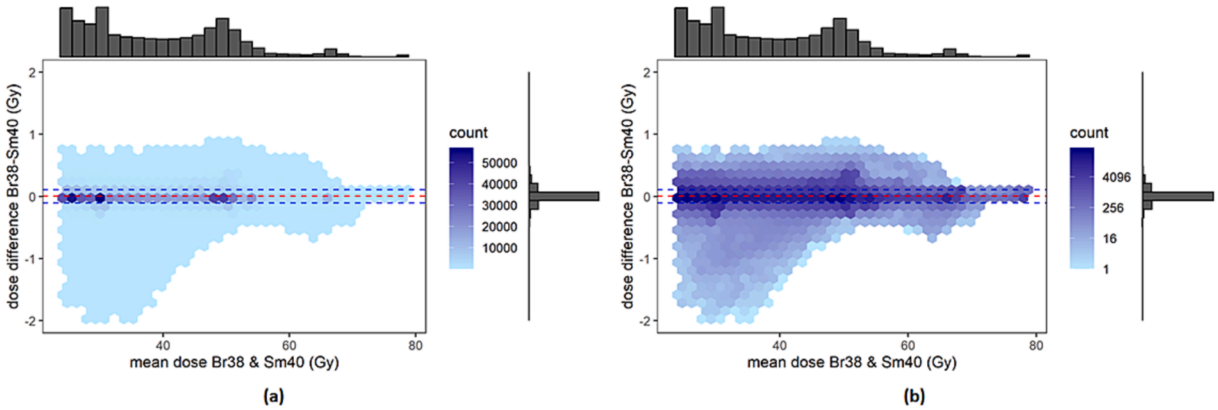

Fig. 3. Bland–Altman plots of the absolute dose difference for all treatment plans. The 95% Limits of Agreement of + –0.1 Gy are presented as blue dashed lines. (a) The image shows a linear scale. (b) The heat map represents a log2 scale to accentuate differences. There was no statistical significant bias. (For interpretation of the references to colour in this figure legend, the reader is referred to the web version of this article.)

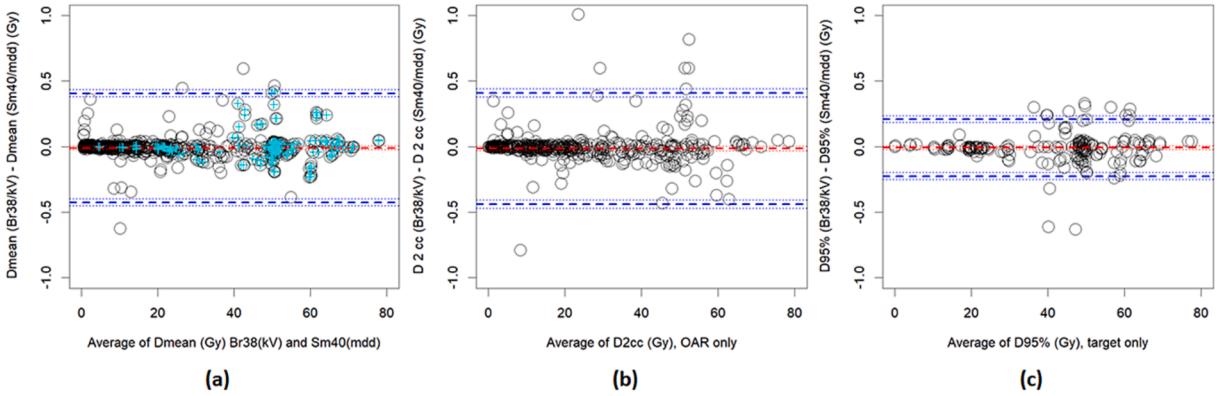

Fig. 4. Bland–Altman plots of the absolute dose difference for dose values of interest. The blue dotted lines represent the 95% limits of agreement whilst the red dashed line represents the bias. (a) The graph represents the difference in mean dose between both methods for all targets (accentuated by blue crosses) and Organs At Risk. (b) The graph shows the difference between both methods for D2cc for OAR only. (c) The graph shows the D95% for targets only. (For interpretation of the references to colour in this figure legend, the reader is referred to the web version of this article.)

4. Discussion

The dose differences between the Br38/kV and Sm40/MD methods were minimal in vivo, without statistically significant bias. 95% LOAs were + –0.05 g/cm^3 and + –0.1 Gy for density and dose, respectively. The results indicated small differences in interface and high–gradient density regions. Our results are in line with the literature, albeit with slightly larger dose differences in vivo compared to phantom results (using mostly electron density) [10,21,22] or other dose calculation algorithms using two different CT scans [13].

CS (Precision) produced more important differences than CC (RayStation) between the Br38/kV– and Sm40/MD–based calculations. However, this was not because of the different dose calculation grids, as shown in Supplementary File S3. Also, to our knowledge, both dose calculations were based on dose–to–water calculations [9]. The origin was suspected to be due to a difference in the buildup and scatter calculations combined with small differences between Br38/kV and Sm40/MD in the interface regions. This was most exacerbated for breast treatments: high doses close to buildup regions combined with tangential fluence and high–density gradient interfaces were in high–dose regions such as the skin and lung. This was most likely due to a) dose calculated in air, b) the small density difference in the buildup region leading to different exit and lateral scattered doses, and c) differences in immobilization device density conversions. These small differences in dose buildup are clinically irrelevant because the optimized PTV regions regularly follow a 3 mm retraction. Further differences between TPS dose calculations were outside the scope of this study. Finally, we believe that the absolute dose correspondences were excellent, with very good agreement between both methods: as shown in the supplementary files S1, the use of a different density phantom for calibration can introduce errors of the same magnitude.

For case 14, density differences were present owing to a different representation of post–contrast injection in specific contrast–enhanced regions (such as the aorta and heart). This was due to a difference in contrast agent injection practice. Injection is performed in one or two phases depending on disease [23,24]. Injection for case 14 concerned a single phase injection followed immediately by the CT scan. This resulted in a high contrast agent concentration in the heart and great vessels present during acquisition, close to the target volume. This was also visible in the D_{2cc} for OARs; the outliers indicated in Fig. 5 were mostly due to this case, thus enlarging the 95% LOAs. The general literature consensus, and also our practice, is that the presence of

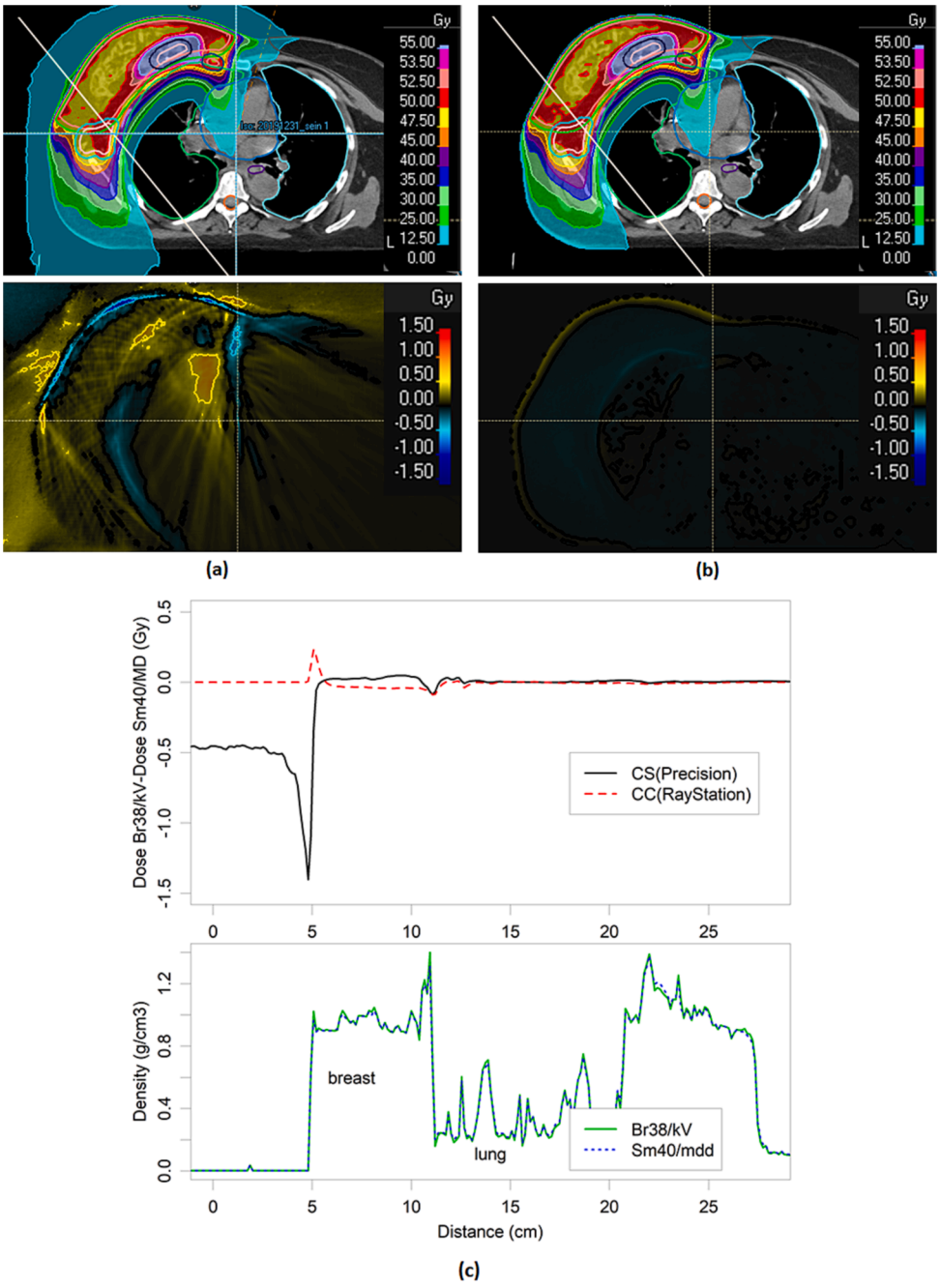

Fig. 5. Profile differences for a same plan between different algorithms and CT representations for a Breast case (50 Gy and 60 Gy boost). (a) CS (Precision) and dose difference between Br38/kV and Sm40/MD dose calculations. (b) CC (RayStation) and dose difference between Br38/kV and Sm40/MD dose calculations. (c) Line profiles of dose differences and density representations. The black line represents the dose difference between both density conversion methods for CS calculations, whereas the red dashed line represents the differences between both density methods for CC calculations. Lower graph: corresponding density profile where small differences can be noted in density gradient regions, finally leading to clinically irrelevant dose differences between density conversions. (For interpretation of the references to colour in this figure legend, the reader is referred to the web version of this article.)

contrast agent only influences very slightly [4,5] and is clinically not relevant as otherwise a second CT scan would have to be acquired, which may lead to registration and movement issues. However, in this specific case 14, a density override in heart and vessels could have improved dose calculation accuracy. Because the density representation for Sm40/MD was, in absolute terms, lower than the Br38/kV representation, this led to a better representation than Br38/kV when not applying a density override for such extreme case.

This study has some limitations. First, there was a lack of radiation oncologist's image quality assessment for contouring directly on the MD images. Generally speaking, radiation oncologists considered contrast slightly inferior for contouring compared to the Br38 (kV) image. Qualitatively speaking for contouring, artifacts due to dense bone, and thus beam hardening, were visually less important for Sm40/MD images, probably due to the explicit differentiation between bone and water.

A future improvement could be the combination of the studied method (MD from a scanner) with binning in material composition (method c as outlined in the introduction). This should be more robust, as the scanner dependency is no longer present.

MD reconstruction using the CT scanner was validated in vivo for clinical application. We showed that phantom verification underestimated in vivo uncertainty, and could introduce a small statistically significant, but clinically not significant, bias for high densities, depending on the used calibration phantom. However, in vivo agreement remained excellent.

In clinical practice, this offers the use of a single image quality–oriented scan with an appropriate kV/FOV for contouring and Sm40/MD reconstruction for dose calculations with less possibility of erroneous conversion curve attributions.

Declaration of Competing Interest

The authors declare that they have no known competing financial interests or personal relationships that could have appeared to influence the work reported in this paper.

Appendix A. Supplementary data

Supplementary data to this article can be found online at https://doi.org/10.1016/j.phro.2023.100463.

References

[1] Geurts MW, Jacqmin DJ, Jones LE, Kry SF, Mihailidis DN, Ohrt JD, et al. AAPM Medical physics practice guideline 5.b: Commissioning and QA of treatment planning dose calculations—Megavoltage photon and electron beams. J Appl Clin Med Phys. 2022. 23. e13641. https://doi.org/10.1002/ACM2.13641.

[2] Mutic S, Palta JR, Butker EK, Das IJ, Huq MS, Loo LND, et al. Med Phys 2003;30:2762–92. https://doi.org/10.1118/1.1609271.

[3] McCollough CH, Boedeker K, Cody D, Duan X, Flohr T, Halliburton SS, et al. Principles and applications of multienergy CT: Report of AAPM Task Group 291. Med Phys 2020;47:e881–912. https://doi.org/10.1002/MP.14157.

[4] Shibamoto Y, Naruse A, Fukuma H, Ayakawa S, Sugie C, Tomita N. Influence of contrast materials on dose calculation in radiotherapy planning using computed tomography for tumors at various anatomical regions: A prospective study. Radiother Oncol 2007;84:52–5. https://doi.org/10.1016/j.radonc.2007.05.015.

[5] Zhang J, Wang L, Xu B, Huang M, Chen Y, Li X. Influence of Using a Contrast-Enhanced CT Image as the Primary Image on CyberKnife Brain Radiosurgery Treatment Plans. Front Oncol 2021;11:705905. https://doi.org/10.3389/FONC.2021.705905.

[6] Cozzi L, Fogliata A, Buffa F, Bieri S. Dosimetric impact of computed tomography calibration on a commercial treatment planning system for external radiation therapy. Radiother Oncol 1998;48:335–8. https://doi.org/10.1016/S0167-8140(98)00072-3.

[7] Kry SF, Feygelman V, Balter P, Knöös T, Charlie Ma CM, Snyder M, et al. AAPM Task Group 329: Reference dose specification for dose calculations: Dose-to-water or dose-to-muscle? Med Phys 2020;47:e52–64. https://doi.org/10.1002/mp.13995.

[8] Knöös T, Nilsson M, Ahlgren L. A method for conversion of hounsfield number to electron density and prediction of macroscopic pair production cross-sections. Radiother Oncol 1986;5:337–45. https://doi.org/10.1016/S0167-8140(86)80183-9.

[9] Reynaert N, Crop F, Sterpin E, Kawrakow I, Palmans H. On the conversion of dose to bone to dose to water in radiotherapy treatment planning systems. Phys Imaging Radiat Oncol 2018;5:26–30. https://doi.org/10.1016/J.PHRO.2018.01.004.

[10] Flatten V, Friedrich A, Engenhart-Cabillic R, Zink K. A phantom based evaluation of the dose prediction and effects in treatment plans, when calculating on a direct density CT reconstruction. J Appl Clin Med Phys 2020;21:52–61. https://doi.org/10.1002/ACM2.12824.

[11] Nelson G, Pigrish V, Sarkar V, Su FC, Salter B. Technical Note: The use of DirectDensityTM and dual-energy CT in the radiation oncology clinic. J Appl Clin Med Phys 2019;20:125–31. https://doi.org/10.1002/ACM2.12546.

[12] Yasui K, Muramatsu R, Kamomae T, Toshito T, Kawabata F, Hayashi N. Evaluating the usefulness of the direct density reconstruction algorithm for intensity modulated and passively scattered proton therapy: Validation using an anthropomorphic phantom. Phys Medica 2021;92:95–101. https://doi.org/10.1016/J.EJMP.2021.11.008.

[13] van der Heyden B, Öllers M, Ritter A, Verhaegen F, van Elmpt W. Clinical evaluation of a novel CT image reconstruction algorithm for direct dose calculations. Phys Imaging Radiat Oncol 2017;2:11–6. https://doi.org/10.1016/J.PHRO.2017.03.001.

[14] Ritter A, Mistry N. DirectDensity ™ n.d. https://cdn0.scrvt.com/39b415fb07de4d9656c7b516d8e2d907/1800000003573122/0964238db26f/RO_SomatomConfidence_Whitepaper_DirectDensity_1800000003573122.pdf (accessed January 15, 2023).

[15] Lu H-M. Raystation dose calculation algorithms n.d. https://www.raysearchlabs.com/siteassets/about-overview/media-center/wp-re-ev-n-pdfs/white-papers/white-paper-7\mathord{-} -dose-calculation-aug-2015.pdf (accessed February 10, 2022).

[16] Gomà C, Almeida IP, Verhaegen F. Revisiting the single-energy CT calibration for proton therapy treatment planning: a critical look at the stoichiometric method. Phys Med Biol 2018;63:235011. https://doi.org/10.1088/1361-6560/aaede5.

[17] Bland JM, Altman DG. Statistics notes: Measurement error. BMJ 1996;312:1654. https://doi.org/10.1136/bmj.312.7047.1654.

[18] Martin Bland J, Altman DG. Statistical methods for assessing agreement between two methods of clinical measurement. Lancet 1986;327:307–10. https://doi.org/10.1016/S0140-6736(86)90837-8.

[19] Bland JM, Altman DG. Measuring agreement in method comparison studies. Stat Methods Med Res 1999;8:135–60. https://doi.org/10.1177/096228029900800204.

[20] Giavarina D. Understanding Bland Altman analysis. Biochem Medica 2015;25:141–51. https://doi.org/10.11613/BM.2015.015.

[21] Feliciani G, Guidi C, Belli ML, D'Errico V, Loi E, Mezzenga E, et al. The Role of a DirectDensity® CT Reconstruction in a Radiotherapy Workflow: A Phantom Study. Appl Sci. 2022. Vol 12. Page 7845. 2022. 12. 7845. https://doi.org/10.3390/APP12157845.

[22] Shutler A, Sarkar A, Grousset G, Shah J, Mourtada F. Evaluation of the Direct Density Algorithm for Energy - Independent Radiotherapy Treatment. Planning 2020:1–20.

[23] Bae KT. Intravenous contrast medium administration and scan timing at CT: Considerations and approaches. Radiology 2010;256:32–61. https://doi.org/10.1148/radiol.10090908.

[24] Caschera L, Lazzara A, Piergallini L, Ricci D, Tuscano B, Vanzulli A. Contrast agents in diagnostic imaging: Present and future. Pharmacol Res 2016;110:65–75. https://doi.org/10.1016/j.phrs.2016.04.023.